ACS OMEGA

Open Access

http://pubs.acs.org/journal/acsodf

Article

MnO_2 Nanoflowers Electrodeposited on Vertically Aligned CNTs as Binder-Free Electrodes for High-Rate Supercapacitors

Mahesh Nepal, Ganesh Sainadh Gudavalli, and Tara P. Dhakal*

Cite This: *ACS Omega* 2025, 10, 3439−3448

Read Online

ACCESS | Metrics & More | Article Recommendations

ABSTRACT: Supercapacitors are gaining attention for their ability to deliver rapid energy discharge while maintaining a high energy storage capacity, effectively bridging the gap between capacitors and batteries. In this paper, we report the performance of a high-capacity, fast-charging, and reliable supercapacitor consisting of nanoflower-like manganese dioxide (MnO_2) decorated on CVD-grown carbon nanotube (CNT) electrodes fabricated using a simple and efficient room-temperature electrodeposition method. The binder-free, self-supporting MnO_2@CNT composite electrodes formed on a flexible carbon fabric demonstrated excellent electrochemical energy storage capabilities, as confirmed by cyclic voltammetry (CV) and galvanostatic charge−discharge (GCD) experiments. The MnO_2 loading significantly affected the electrode's capacity, with the highest specific capacitance of 219 F g^{-1} achieved at low mass loading (3.37 mg cm^{-2}) and the highest areal capacitance of 1.5 F cm^{-2} for high mass loading (15.6 mg cm^{-2}). The rectangular curve observed in CV experiments at faster scan rates (5−50 mV s^{-1}) and the triangular curve observed in the GCD experiment at high current densities (0.1 to 0.5 A g^{-1}) demonstrate the high-rate capability of the MnO_2@CNT electrode. The electrode also showed outstanding stability, retaining 88% of its initial capacity after 7000 cycles. Electrochemical impedance spectroscopy (EIS) measurement and corresponding analysis of the data indicated fast charge transfer kinetics and facile ion diffusion into the MnO_2 electrode, which is attributed to the nanoflower-like structure of MnO_2 formed on porous carbon nanotubes, leading to excellent rate performance. With these advancements, our MnO_2@CNT supercapacitors have significant potential in electric vehicles, complementing batteries by enabling fast discharge for quick acceleration.

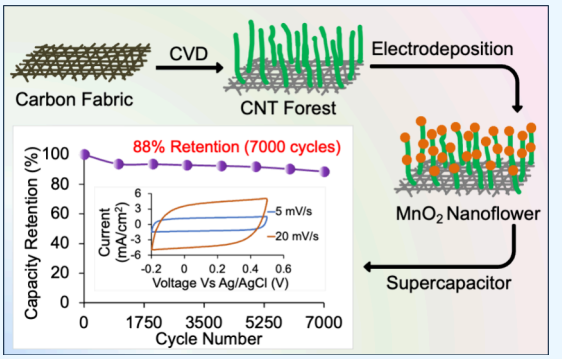

INTRODUCTION

Supercapacitors combine the properties of both capacitors, which can deliver energy in very short time, and batteries, which can store large amount of energy.[1] Hybrid supercapacitors use a composite of carbonaceous materials, such as activated carbon and highly conductive carbon nanotubes, and transition metal oxides, such as manganese oxide and ruthenium oxides, in order to greatly improve the electrochemical performance. The enhanced performance comes from the combined effect of the double layer charge storage mechanism of carbonaceous materials and the pseudocapacitive nature of the transition metal oxides. In this paper, CNTs are used as the electric double layer capacitor (EDLC)-type materials combined with the pseudocapacitive-type material MnO_2. The physical properties of the substrate electrodes such as microstructure, surface area, and pore size affect the nature of deposited MnO_2; hence, CNTs are ideal to achieve superior performance.[2]

In pure EDLC, charge is stored electrostatically at the interface between the electrode and electrolyte, similar to parallel plate capacitors, without any chemical interaction between the electrode and ions. The distinction between a parallel plate capacitor and EDLC lies in the distribution of charges. In a parallel plate capacitor, opposite charges reside on the two metal electrodes, whereas in an EDLC, one charge resides on the electrode, while its opposite counterpart is present in the electrolyte. The advantage of EDLC over a parallel plate capacitor is that it allows for the utilization of electrodes with very high surface areas. This is made possible by the use of an electrolyte that can penetrate extremely porous electrodes, unlike parallel plate capacitors, which use solid dielectrics such as ceramics, paper, or mica and require planar electrodes. The increased surface area of the electrodes results in significantly higher capacitance in EDLCs, as the capacitance is directly proportional to the area. Therefore, electrodes with a very high surface area, such as activated

Received: August 8, 2024
Revised: January 12, 2025
Accepted: January 16, 2025
Published: January 27, 2025

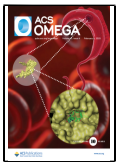

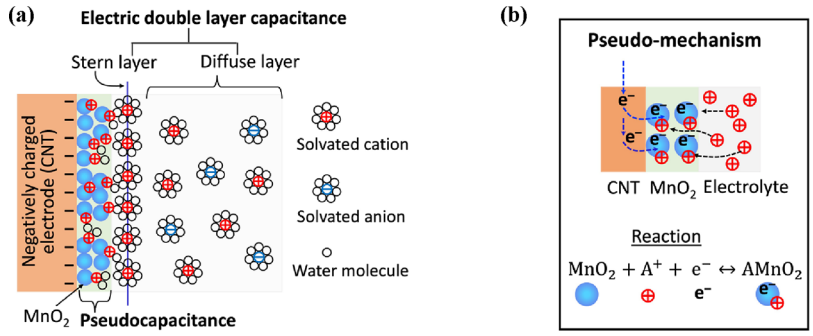

Figure 1. (a) Illustration of simultaneous pseudocapacitance and electric double layer capacitance (EDLC) mechanisms: The MnO_2 layer stores charges through a faradaic redox reaction during ion intercalation, while high-surface-area electrodes like CNT contribute to the EDLC mechanism by forming two ionic layers in the electrolyte—an inner compact layer representing the Stern layer and an outer layer representing the diffuse layer. Adapted in part with permission from ref 3. (b) Detailed depiction of the pseudocapacitive mechanism.

carbon or CNTs, are desirable. The term "double layer" comes from the fact that when voltage is applied across the EDLC, there is a buildup of two layers of electric charge near each electrode upon charging. Figure 1a shows two regions (layers) of ion distribution—the inner region called the compact layer or Stern layer, and the outer region called diffuse layer.[3] These two distinct layers give rise to the term "electric double layer". The Stern layer is the closest layer of ions to the electrode surface, comprising either positive or negative ions that are opposite in charge to the electrode and specifically adsorbed onto the surface. The ions are attracted to the electrode by electrostatic forces and form a tightly bound layer, making them relatively immobile. The charges in the electrode and the ions in the stern layer are separated by only one or a few solvent molecules (such as H_2O in the case of an aqueous electrolyte), which act as a dielectric material. This results in a dielectric thickness in the range of a few Å, leading to very high capacitance, since dielectric thickness is inversely proportional to capacitance. The diffuse layer is the region extending beyond the Stern layer comprising ions of mixed charge, with some being attracted to the stern layer and others to the electrode. These ions are less tightly bound and mobile and form a continuous distribution throughout the electrolyte due to thermal motion. The overall capacitance of the EDLC is determined by the combined effect of both layers.

On the contrary, pseudocapacitance as depicted in Figure 1b is characterized by rapid and reversible faradaic reactions, facilitating swift charge transfer.[4] This exchange happens between the electrode and ions both adsorbed on the surface and intercalated within a specific depth of the electrode. Unlike batteries, pseudocapacitive materials undergo charging and discharging processes in a remarkably brief duration owing to the rapid and reversible faradaic electron-charge transfer. The term "pseudocapacitive" denotes the unique nature of these materials; although they involve charge transfer, their capacitive behavior is evident in galvanostatic charge–discharge (GCD) and cyclic voltammetry (CV) curves. Notably, the CV curve exhibits a rectangular shape, while the GCD curve assumes a triangular form, just like traditional capacitors. Common examples of pseudocapacitive materials include metal oxides like RuO_2,[5] MnO_2,[6,7] NiO,[8] and Co_3O_4,[9] metal sulfides such as MoS_2[10] and TiS_2,[11] and conducting polymers such as polypyrrole (PPy)[12] and polyaniline (PANi).[13] Recently, MXenes—two-dimensional advanced nanomaterials—have emerged as promising candidates for pseudocapacitance applications due to their unique layered structures, which enhance electrolyte ion transport and provide active redox sites on the surface.[14−16]

We have used MnO_2 as our pseudocapacitive material due to its low cost, environmentally friendly nature, and ease of fabrication, particularly for decorating over our carbon nanotube (CNT) electrode.[17] The pseudocapacitive behavior of MnO_2 was initially discovered by Lee and Goodenough in 1999 while investigating the properties of amorphous $MnO_2 \cdot nH_2O$ in a KCl aqueous electrolyte.[18] In an aqueous electrolyte, the pseudocapacitive behavior of MnO_2 arises from the transfer of charges, primarily attributed to the redox process of manganese ions (Mn) transitioning between their +4 and +3 oxidation states, as visually represented in Figure 1. In the context of charge storage mechanisms in MnO_2, two simultaneous mechanisms have been proposed to elucidate this phenomenon as depicted below, where A^+ denotes the cations present in the electrolyte, e^- represents electrons, and x denotes the fraction of cations per MnO_2 molecule. The value of x can vary, with a tendency for it to be closer to 1 at the surface and decrease as the depth increases. This trend arises because it becomes challenging for cations to intercalate deeper into the MnO_2 structure.

$$(MnO_2)_{surface} + A^+ + e^- \leftrightarrow (MnO_2^- A^+)_{surface} \quad (1)$$

$$MnO_2 + xA^+ + xe^- \leftrightarrow A_xMnO_2 \quad (2)$$

Equation 1 illustrates the first mechanism wherein metal cations (A^+) from the solution adsorb onto the surface of MnO_2 during charging (forward reaction) and then release back into the electrolyte during discharging (reverse reaction). In eq 2, the second mechanism involves cations (A^+) from the solution intercalating into the bulk of MnO_2 while charging and then slipping out during discharging. In both processes, manganese's oxidation state toggles between +3 and +4.[18,19]

Due to its semiconducting nature, the conductivity of MnO_2 is significantly lower than that of carbon-based materials, ranging from 10^{-7} to 10^{-3} S cm^{-1}.[17] As the loading of MnO_2 increases, there is a notable decrease in specific capacitance (F g^{-1}). So, thinner MnO_2 films are desirable to improve electrical conductivity and ion diffusion by reducing resistance in charge transfer and shortening diffusion paths, enhancing efficiency in embedding and removing charges and ions from the material body. However, thinner films lead to a decreased areal capacitance (F cm^{-2}), a crucial consideration for practical applications. To overcome this limitation and simultaneously improve the conductivity and cycling stability of MnO_2, the

https://doi.org/10.1021/acsomega.4c07287
ACS Omega 2025, 10, 3439−3448

development of composite electrodes presents a promising solution. Carbon materials, including CNTs, graphene, porous carbon, carbon nanofibers, and carbon aerogel, are commonly utilized for composite electrode due to their high specific surface areas and conductivity.[20] Various methods have been employed to incorporate MnO_2 into nanoscopic carbon, including physical mixing of components,[21] redox reaction,[22] electrodeposition,[23,24] sol−gel process,[25] hydrothermal method,[26] RF sputtering,[27] and others.[28,29] The specific capacitance of MnO_2 electrodes varies depending on the method of synthesis, as well as the nanostructures used. For instance, Zhang et al.[24] fabricated MnO_2/CNT composites via electrodeposition, achieving high capacity (199 F g^{-1}, ∼1 A g^{-1}), excellent rate capability (50.8%, 77 A g^{-1}), and long cycle life (20,000 cycles). On the other hand, Li et al.[28] employed a modified chemical method in a mild one-pot reaction process to attach the cross-linked MnO_2 layer onto the sidewalls of inner CNTs. The composite demonstrates a higher specific capacitance (201 F g^{-1} at 1 A g^{-1}) and improved rate capability (140 F g^{-1} at 20 A g^{-1}). Likewise, the MnO_2/carbon aerosol heterostructure, fabricated by Liu et al.[29] using the sol−gel method, exhibited a specific capacitance of 384 F g^{-1} at a current density of 0.5 A g^{-1}.

In this study, we employed a facile electrodeposition method to grow MnO_2 conformally onto CNTs, which were, in turn, grown on carbon fabric via the common CVD process. The vertically aligned structure of the CNTs not only provides an efficient pathway for electron conduction but also facilitates effective loading of MnO_2 onto the porous electrode, resulting in a high areal capacity. Additionally, the hierarchical porous nanoflower structure of the electrodeposited MnO_2 promotes rapid ion diffusion from the surface to the interior, maximizing the utilization of active materials. Moreover, the self-supporting nature of this electrode eliminates the need for a binder, which would have added unnecessary weight and reduced the capacitance density. The resulting symmetric supercapacitor device exhibited an areal capacitance of 1.5 F cm^{-2} for high mass loading (15.6 mg cm^{-2}).

EXPERIMENTAL SECTION

Materials and Chemicals. Carbon fabric (CF) purchased from Zoltek (99% carbon content, weight = 115 g m^{-2}, thickness = 406 μm, electrical resistivity = 0.0014 Ω·cm, density = 1.75 g cc^{-1}) was used as a substrate, which is a binder-free and plain weave carbonized woven fabric. The atomic layer deposition (ALD) precursor for alumina deposition was trimethylaluminum (TMA) purchased from Strem Chemicals. Carbon-containing gas used during CNT growth was ethylene, which was purchased from Airgas, and the chemical used for MnO_2 deposition was $MnSO_4{\cdot}5H_2O$ purchased from Sigma-Aldrich.

Electrode Fabrication. The electrode fabrication process began with the selection of woven CF as the substrate due to its lightweight, flexibility, and expansive surface area. It also serves as a current collector due to its good conductivity. The CF consists of interwoven carbon fibers, forming a microstructured network. Although copper and aluminum foil are commonly used as current collectors in many electrochemical cells, we chose carbon fabric to promote CNT growth in hedge-like patterns along the individual fibers, creating a more porous and efficient structure for supercapacitors. Initially, the CF fabrics were precisely cut into pieces measuring 2 in. × 1 in. Subsequently, a thorough cleaning was implemented, involving sequential treatments with acetone, ethanol, and DI water. Upon completion of the cleaning process, the substrates were promptly transferred to a furnace and heated in an N_2 ambient temperature at 100 °C for 30 min to ensure thorough drying. After cleaning, an alumina buffer layer was deposited on CF substrates using ALD at a deposition rate of 1 Å/cycle at a temperature of 200 °C.[30] This alumina buffer layer acts as a diffusion barrier for both the catalyst and incoming carbon species at high temperatures. A thin film of 5 nm Fe was then deposited as a catalyst on the alumina-coated CF by using magnetron sputtering at a deposition rate of approximately 0.5 Å/s. The purpose of the catalyst is to facilitate the growth of CNTs by providing active sites where a carbon-containing gas breaks down, diffuses through it, and precipitates as CNTs upon supersaturation. Following this, CNTs were synthesized using the water-assisted chemical vapor deposition (WA-CVD) technique at 800 °C using ethylene gas.[31,32] The process involves (a) placing Fe@Al_2O_3-coated carbon fiber (CF) samples in the center of a quartz tube within the furnace for accurate temperature control, (b) flushing the tube with 500 sccm of a forming gas (5% H_2/95% Ar) for 30 min to ensure an oxygen-free environment, (c) heating the tube reactor to 800 °C at a rate of ∼1 °C/s, and (d) maintaining the temperature at 800 °C for 10 min to convert the metal catalyst into nanoparticles. This is followed by initiating an ethylene (C_2H_4) gas flow to the reactor. After 3 min, water (H_2O) was bubbled to the reactor using forming gas. The H_2O molecules removed amorphous carbon from the active catalyst, thereby increasing the catalyst's lifetime. During the CNT growth, the flow rate of the forming gas, H_2O, and C_2H_4 were 200, 50, and 20 sccm, respectively. The growth was terminated after 2 h followed by turning off the furnace while maintaining the forming gas flow at 500 sccm until the furnace cooled to room temperature. The sample was then removed and weighed to estimate the amount of the CNTs deposited. Upon synthesis, the CNTs underwent treatment with acid to remove catalyst particles and introduce surface carboxylic groups (−COOH, −OH, and >C═O),[33−35] which not only enhance pseudocapacitance but also render the CNTs hydrophilic, thereby improving the accuracy of electrochemical measurements.[36]

To deposit MnO_2 conformally onto the CNT@CF substrate, we employed a galvanic electrodeposition. A three-electrode system was set up using the Solartron 1287 electrochemical interface. A 0.2 M $MnSO_4$ solution served as the MnO_2 source. To maintain a pH of 6 in the solution, we added dilute sulfuric acid. Electrodeposition at pH 6 is known to enhance the performance of manganese oxide in electrochemical capacitor applications.[6,37] The coating process employed square-wave pulse with 10 s "on time" and 10 s "off time" for each duty cycle, at a current density of 4 mA cm^{-2}. The loading of MnO_2 was controlled by varying the number of square waves and determining the deposition time. Three different electrodes were fabricated with 65, 130, and 390 square waves, representing increasing levels of MnO_2 loading. Following deposition, the samples were dried overnight in a N_2 atmosphere before undergoing electrochemical analysis. The weight of the substrates before and after MnO_2 deposition was measured using a Sartorius microbalance with a measurement accuracy of 10 μg, enabling accurate determination of the active mass of MnO_2 involved in charge storage for specific capacitance calculations.

Electrochemical Measurements and Characterizations. The Solartron 1287 electrochemical interface served

https://doi.org/10.1021/acsomega.4c07287
ACS Omega 2025, 10, 3439−3448

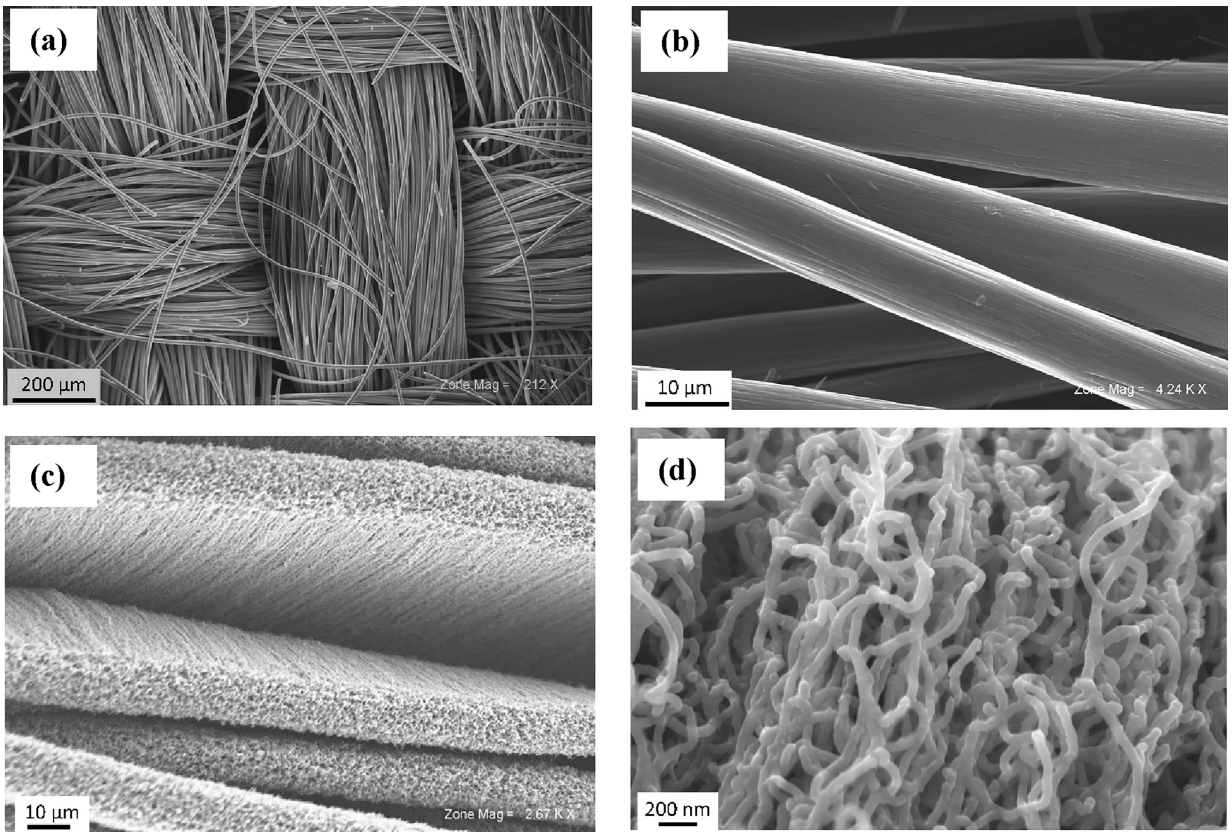

Figure 2. SEM images of (a) bare carbon fabrics, (b) carbon fiber strands showing a smooth surface, and (c, d) high-density CNTs forest on carbon fabric with height around 150 μm at different magnifications.

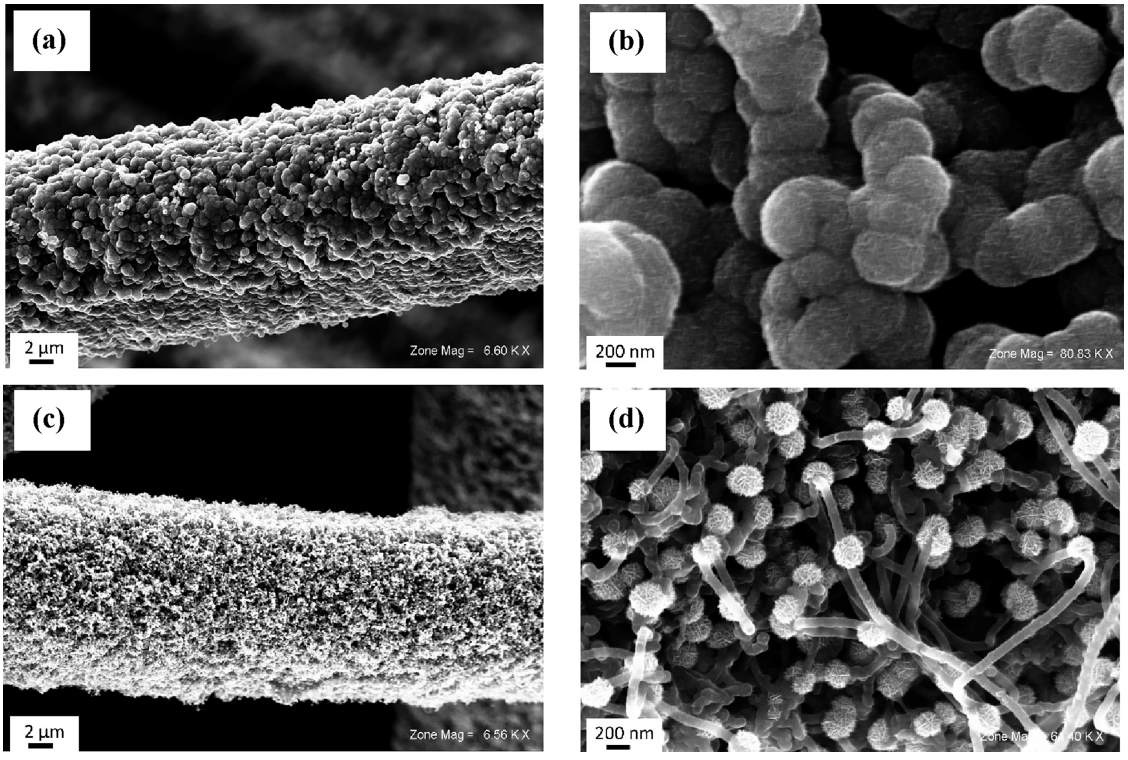

Figure 3. SEM images of MnO_2 electrodeposited on CNT@CF at (a) a current density of 4 mA cm^{-2} for 65 square waves and (b) its zoomed-in picture showing thick MnO_2 growth in a lump fashion, and (c) at 1 mA cm^{-2} for 130 square waves and (d) its close-up showing sparsely populated blobs of MnO_2 nanoflowers on the walls of CNT.

https://doi.org/10.1021/acsomega.4c07287
ACS Omega 2025, 10, 3439−3448

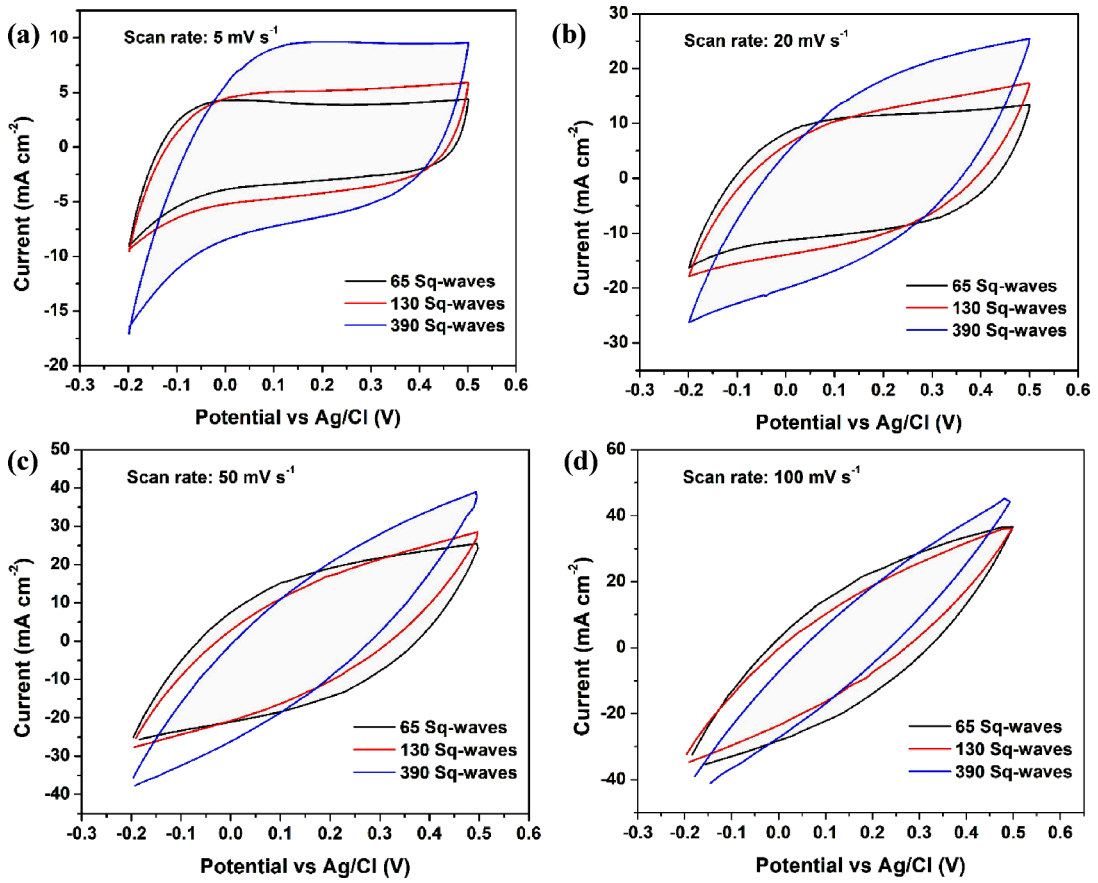

Figure 4. CV scans of MnO_2@CNT@CF electrodes with different loading of MnO_2 represented by 65 square waves, 130 square waves, and 390 square waves at different scan rates (a) 5 mV s^{-1}, (b) 20 mV s^{-1}, (c) 50 mV s^{-1}, and (d) 100 mV s^{-1}.

as the primary tool for electrochemical characterization, employed in both half-cell (three-electrode system) and full cell (symmetric) configurations. In the standard three-electrode setup, the working electrode consisted of MnO_2 on CNT@CF, with a platinum (Pt) plate serving as the counter electrode and an Ag/AgCl reference electrode (3.5 M KCl, 0.207 V vs standard hydrogen electrode, SHE). All electrochemical measurements were conducted by using 0.5 M Na_2SO_4 in DI water as the electrolyte. To assess the electrochemical performance of the MnO_2@CNT@CF electrode, CV, GCD, and electrochemical impedance spectroscopy (EIS) techniques were employed. For life cycle testing, coin cells were assembled and cycled by using an Arbin coin cell tester.

RESULTS AND DISCUSSION

Morphology of the Electrodes. Figure 2a shows the nicely woven structure of bare CF substrate, and Figure 2b is the zoomed-in picture showing the structure of bare CFs of around 10 μm diameter. Figure 2c shows the SEM image of the CNTs that are grown on CFs with thicknesses of about 150 μm in height. Figure 2d shows a close-up of the top surface of the CNT forest grown on the fibers. The CNTs are well adhered to the CFs and are of very high surface area and appear densely packed. Each CNT diameter is about 50 nm, indicating they are multiwalled carbon nanotubes (MWCNTs). It is proven that single-walled carbon nanotubes (SWCNTs) have smaller diameters (0.5−2.5 nm), while multiwalled CNTs tend to be larger, depending on the number of walls.[38] High-resolution transmission electron microscopy (HR-TEM) conducted by our previous group confirmed the presence of MWCNTs (~11 walls per tube) when using the similar procedure to grow CNTs.[39] Additionally, our recent work using the same CVD process to grow MWCNTs for Li-ion battery anode showed a characteristic D-band in the Raman spectrum.[31] This D-band arises from defects in the MWCNTs, which may serve as additional adsorption sites.

Figure 3a shows the SEM image of manganese oxide electrodeposited on the CNT@CF at 4 mA cm^{-2} with 65 square waves.[40] It clearly shows that the electrodeposited manganese oxide has completely covered the CNT by growing in a lump fashion. A close-up picture of one of the lumps of MnO_2 in Figure 3b shows the nanoflower structure consisting of many nanoflakes. In order to understand the growth precisely, MnO_2 was electrodeposited at a lower current density of 1 mA cm^{-2} for 130 square waves. The SEM image of the MnO_2 grown around CNT strands is shown in Figure 3c,d. Interestingly, sparsely populated almost spherical MnO_2 blobs of around 150 nm diameter have been observed with quite a high consistency. The MnO_2 blobs around the CNTs have a flower-like structure with hierarchy, i.e., the core starts at one point on the CNT and the flower grows outward with numerous nanosheets of MnO_2 well adhered to the walls of the CNT due to their morphological stability. The nanoflowers consist of hundreds of nanosheets interwoven together to provide a high surface area. The length and thickness of each nanosheet is about 3 to 50 nm. Similar structures have been

https://doi.org/10.1021/acsomega.4c07287
ACS Omega 2025, 10, 3439−3448

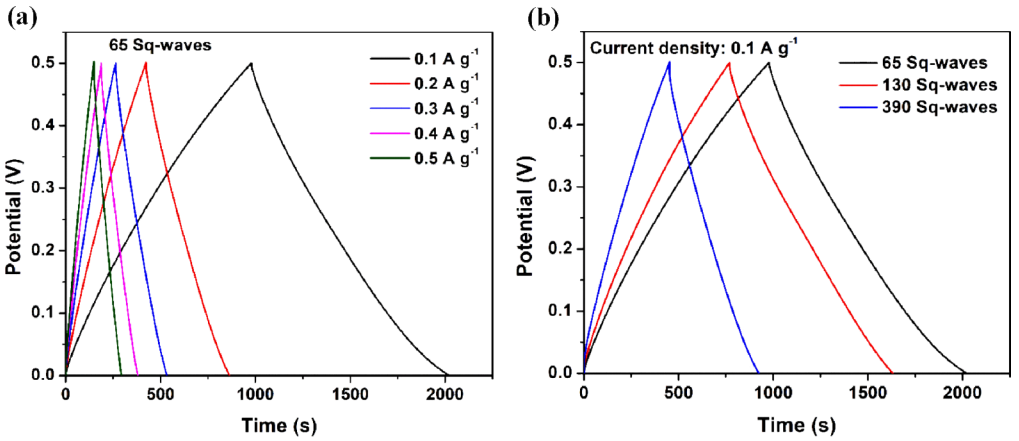

Figure 5. Charge−discharge profile of MnO_2@CNT@CF electrodes in half-cell configuration. (a) Electrode with 65 square waves cycled at different current densities from 0.1 to 0.5 A g^{-1}. (b) Comparison of electrodes with different MnO_2 loadings resulting from 65, 130, and 390 square waves. The longer the charge−discharge time, the higher the capacity.

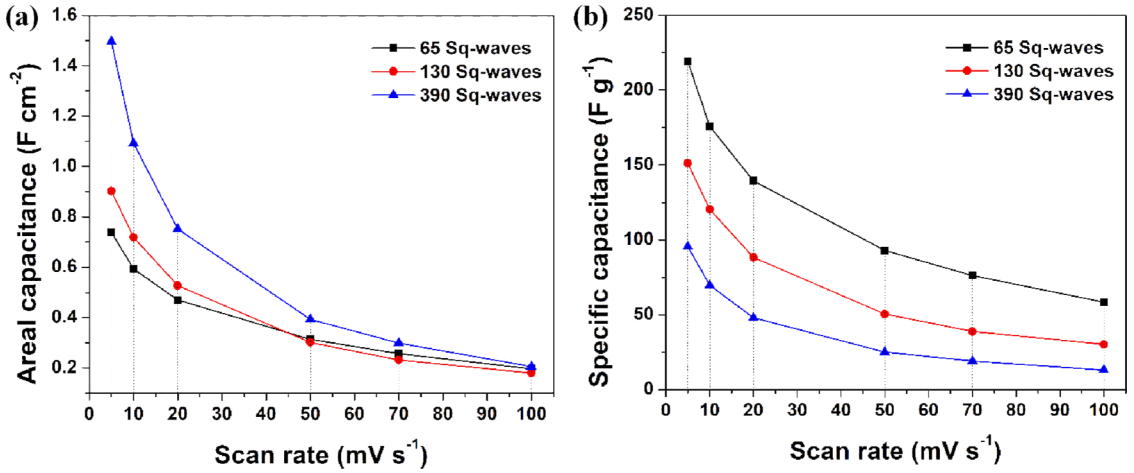

Figure 6. Comparison of (a) areal capacitance (F cm^{-2}) and (b) specific capacitance (F g^{-1}) vs scan rate for all samples (65, 130, and 390 square waves) showing an increase in areal capacitance with higher MnO_2 mass loading while an opposite trend is observed for the specific capacitance.

observed in earlier reports for electrodeposited MnO_2.[41−44] This hierarchical structure contributes toward the high surface area of the electrode material leading to more capacitance. From this observation, we can expect the electrodes with similar morphology but a more densely populated MnO_2 nanoflower for the 130 and 390 square wave samples.

Half-Cell Configurations. CV was performed on MnO_2@CNT@CF electrodes having various loadings of electrodeposited MnO_2 determined by different numbers of square waves starting from 65 to 390 at various scan rates such as 5, 10, 20, 50, 70, and 100 mV s^{-1} between voltages of −0.2 and 0.5 V (i.e., 0.7 V of electrochemical window) in a three-electrode cell. The quasi-rectangular CV plot has been retained for all three samples at a slow scan rate, as shown in Figure 4a,b, indicating good capacitive performance of MnO_2. However, the slope of the curves can be seen increasing at a higher scan rate in Figure 4c,d, which can be related to the increase in equivalent series resistance as we drive the charging/discharging process faster.

In addition, when comparing the area of rectangular CV curves at specific scan rates in Figure 4, there is an increasing trend observed from the electrode with 65 to 390 square waves. This increase in area corresponds to a higher capacitance as indicated by eq 3. The underlying reason for this phenomenon is the proportional mass loading of MnO_2 during electrodeposition, where an increasing number of square waves leads to a greater amount of MnO_2. Consequently, the presence of more MnO_2 results in an increased number of reaction sites, facilitating a higher occurrence of faradaic reactions and resulting in a greater areal capacitance.

The GCD was also performed on three samples at constant current densities of 0.1 to 0.5 A g^{-1} in steps of 0.1 A g^{-1}. The GCD profiles of MnO_2 electrodeposited on CNTs with different square waves are shown in Figure 5. All the GCD profiles are near triangular with no plateaus, indicating very good capacitive characteristics and superior reversibility for the reactions. It can be seen in the GCD plots that the time of discharge is increasing as we go from thicker MnO_2 (390 square waves) to thinner MnO_2 (65 square waves), indicating an increase in specific capacitance (F g^{-1}) for the electrode with low mass loading.

The areal capacitance (F cm^{-2}) for each sample is estimated from CV curves using eq 3, where $\int_{V1}^{V2} i dV$ is the integrated area of the CV curve with current i in A cm^{-2}, v is the scan rate in mV s^{-1}, and V_1 and V_2 are the initial and final potentials.

https://doi.org/10.1021/acsomega.4c07287
ACS Omega 2025, 10, 3439−3448

$$C(\mathrm{F\ cm^{-2}}) = \frac{\int_{V1}^{V2} i\,dV}{2(V_2 - V_1)\nu} \quad (3)$$

This capacitance was converted into specific capacitance (F g^{-1}) by taking the weight of the active MnO_2 into account. A high mass loading of MnO_2 was used on the electrodes: ∼15.6 mg cm^{-2} for the electrode with 390 square waves, 5.93 mg cm^{-2} for the electrode with 130 square waves, and ∼3.37 mg cm^{-2} for the electrode with 65 square waves. These weights are practical and comparative to the mass loading (∼10 mg cm^{-2}) of commercial supercapacitors.[45] Figure 6 shows the areal capacitance (F cm^{-2}) and specific capacitance (F g^{-1}) vs scan rate for all samples with different mass loadings of MnO_2. At a scan rate of 5 mV s^{-1}, a high areal capacitance of 1.5 F cm^{-2} was achieved for the sample with 390 square waves while the lowest value was 0.7 F cm^{-2} for 65 square waves. This can be attributed to the more active mass loading for a high number of square waves. A decrease in capacitance for all samples can be observed for higher voltage scan rates. As the scan rate increases, the diffusion of electrolyte ions into the electrode internal pore structure becomes difficult (also called diffusion limitation), and the corresponding ineffective interaction between the electrolyte and electrode materials results in reduced specific capacitance. However, contrary to our expectation, there is almost no difference in areal capacitance among all three samples at faster CV scan (especially at 100 mV s^{-1}). This is in contrast to the results of our previous work published in 2019, where we directly loaded MnO_2 onto CF without CNTs.[40] We propose that the low porosity of the CNT forest, after being coated with thick MnO_2, hinders ion diffusion, especially at a fast scan rate. Consequently, only the outer layer of MnO_2 might contribute to the total capacitance, resulting in nearly equal areal capacitance for all three samples regardless of MnO_2 loading. In contrast, our previous work demonstrated that there was enough space available between the CFs, even after MnO_2 coating, allowing for efficient ion movement. Additionally, for comparison, the areal capacitance is also estimated from the GCD curves shown in Figure 5a by multiplying the slope of the discharge curve by the current density. These values closely match the areal capacitances obtained from the CV curves, as shown in Table 1, indicating the accuracy of our experimental results.

Table 1. Comparison of Specific Capacitance Calculated from Cyclic Voltammetry (CV) (at 5 mV s^{-1}) and Galvanostatic Charge−Discharge (GCD) (at 0.1 A g^{-1}) for All Three Samples

no. of square waves (mass loading of MnO_2)	specific capacitance (F g^{-1}) CV vs GCD	areal capacitance (F cm^{-2}) CV vs GCD
65	219/213	0.73/0.72
130	151/182	0.90/1.00
390	95/100	1.5/1.5

Regarding the specific capacitance, a high value of 219 F g^{-1} has been achieved for the sample with 65 square waves of MnO_2. However, the specific capacitance dropped to 58 F g^{-1} at 100 mV s^{-1}, which was a 28% decline. The same trend has been seen in the other three samples with increasing MnO_2 loading, as shown in Figure 6b. The highest specific capacitances of electrodes with 130 and 390 square waves were 151 and 95.5 F g^{-1}, respectively. These values match the specific capacitances obtained from the GCD curves, as shown in Table 1, indicating the accuracy of the measurements. There is a decrease in specific capacitance as the MnO_2 loading increases, contrary to the trend observed for the areal capacitance. This can be attributed to the efficient participation of most Mn atoms in fast and reversible faradaic reactions within the thinner MnO_2 layer. As the MnO_2 loading increases, it becomes more challenging for cations/anions from the electrolyte to diffuse deeper into MnO_2, hindering the redox process and consequently lowering the specific capacitance.

Symmetric Cell Design. The electrode with 65 square waves of MnO_2 was chosen as both anode and cathode in a symmetric capacitor configuration as it demonstrated the maximum specific capacitance in half-cell configuration. Figure 7a shows CV curves between the voltage window of −0.2 V and 0.5 V in 1 M Na_2SO_4 at various scan rates. The CV profiles are closely rectangular shapes without apparent distortion for faster scan rates from 5 to 50 mV s^{-1}, suggesting favorable fast charge and discharge characteristics of the devices. A change from rectangular to oval shapes at slower scan rates (70 and 100 mV s^{-1}) is caused by an increased ion diffusion resistance. The estimated areal capacitance for the symmetric cells, using eq 3, is from 235 mF cm^{-2} for 5 mV s^{-1} to 76 mF cm^{-2} for 100 mV s^{-1}. If we compare these values with the half-cell results, we can observe a reduction in the areal capacity. This reduction is primarily attributed to the electrode placement, wherein the reference electrode was positioned farther away to allow for a closer arrangement of the anode and cathode electrodes, closely resembling a practical device.

Life-cycle testing was carried out at a constant current density of 0.5 A g^{-1} for 7000 cycles to observe the stability in a coin cell configuration. The observed 88% capacity retention after 7000 cycles in Figure 7b shows the great stability of the MnO_2@CNT@CF electrode. During cycling, the MnO_2 films gradually dissolve into the electrolyte, which leads to the loss of active electrode material, resulting in capacitance fading.[46] The inset in Figure 7b demonstrates a real-life application of the supercapacitor, powering a red LED using three supercapacitor coin cells connected in series.

To gain deeper insights into the charge transfer resistance and fast-charging capability of our supercapacitor, the EIS was performed, which is displayed in the form of Nyquist plot in Figure 8a. The EIS was recorded over a frequency range of 100 kHz to 10 mHz. The Nyquist plot shows a nearly vertical line, exhibiting capacitor-like behavior. In comparison, an ideal capacitor, such as ceramic capacitor, would display a perfect straight line parallel to the *y*-axis. To simplify and interpret the complex phenomenon, the EIS plot is modeled with an equivalent circuit, as shown in Figure 8b. The offset of the vertical line from the *y*-axis corresponds to the bulk resistance or series resistance R_b. This resistance is independent of the frequency and can arise from factors like electrode resistance and contact resistance during measurement. The EIS plot at the high-frequency region (inset of Figure 8a) reveals one semicircle with an upward facing feature at the beginning. A similar feature can be observed in the EIS plot taken by Gong et al. for their graphene oxide electrode.[47] The semicircle in the high-frequency region can be modeled by a parallel combination of capacitance, C_{ct}, and resistance, R_{ct}, which represents the charge transfer commonly observed in batteries and supercapacitors. During the redox reaction, which involves the transfer of charge between the ions and the electrode active material, reaction kinetics plays a role in impeding the instantaneous reaction, leading to a certain resistance

https://doi.org/10.1021/acsomega.4c07287
ACS Omega 2025, 10, 3439−3448

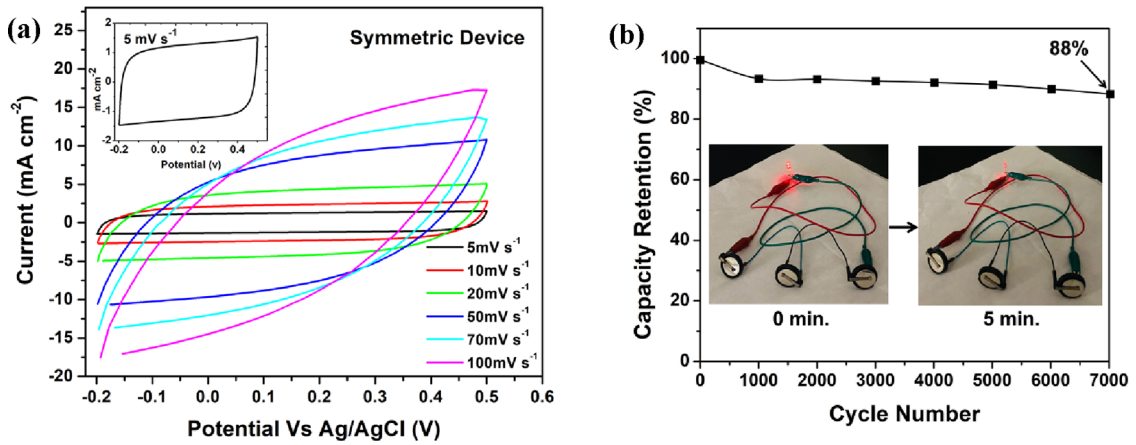

Figure 7. (a) Cyclic voltammetry of a symmetric supercapacitor system tested with both the cathode and anode composed of 65 square waves MnO_2@CNT@CF. The inset shows a near rectangular cyclic voltammetry plot at 5 mV s^{-1}. (b) Cycling stability of a supercapacitor measured at current density of 0.5 A g^{-1} for 7000 cycles with 88% capacity retention. The inset demonstrates a real-life application of supercapacitors powering a red LED.

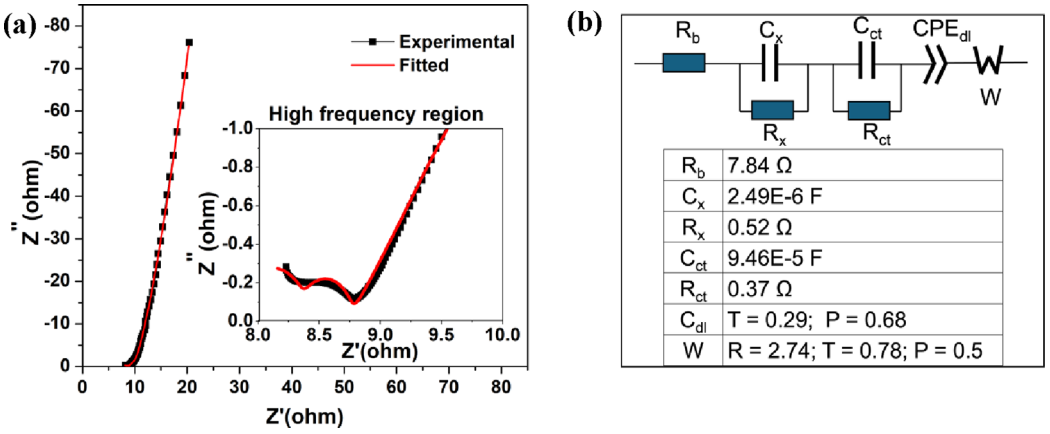

Figure 8. (a) Impedance plot of the symmetric supercapacitor recorded in the frequency range of 100 kHz to 10 mHz with the inset showing the response at high frequencies. (b) Equivalent circuit model, where *R*, *C*, CPE, and *W* represent resistance, capacitance, constant phase element, and Warburg impedance, respectively. The values after fitting the model are provided in the table.

associated with the charge accumulation at the electrode interface. Notably, the R_{ct} is less than an ohm in our case, indicating fast kinetics unlike batteries where this value typically falls within the range of tens of ohm.[48] This reveals that the redox reaction involving MnO_2 is fast, resulting in excellent rate performance characterized by rapid charging and discharging capability.

The unusual feature at the beginning of EIS seems to be an incomplete part of another semicircle represented by parallel C_x/R_x combination, which could complete and come into contact with the *x*-axis if measured at higher frequency. The estimated capacitance for C_x and R_x is 2.49 × 10^{-6} farad and 0.52 ohm, respectively, which should be attributed to a phenomenon occurring on a faster time scale than charge transfer. We hypothesize that electronic transport between the graphene rolls of MWCNTs may have contributed to this effect. Further investigation is needed to better understand this phenomenon. The lower-frequency region in the Nyquist plot is modeled by an EDLC capacitor represented by a constant phase element (CPE_{dl}) in series with Warburg impedance (*W*). The constant phase element is used to account for the imperfect capacitor behavior, as indicated by the nonperfect vertical line in our case. The Warburg impedance arises from the diffusion resistance of ions into the electrode material and is represented by a 45° angled line in the Nyquist plot. However, in our plot, there is no visible 45° region. The value of resistance associated with Warburg impedance is estimated to be only 2.74 ohms, indicating the favorable diffusion of ions into the MnO_2 material. This can be attributed to the flower-like morphology of MnO_2, which provides a porous structure that facilitates ion diffusion. The lower Warburg impedance contributes to the improved rate performance of our electrode, further supporting its excellent performance in high-rate applications.

The charge transfer resistance R_{ct} obtained from the EIS curve fitting is less than an ohm in our case, indicating fast kinetics unlike battery where this could be an order of magnitude higher.[48] This reveals that the redox reaction involving MnO_2 is fast, resulting in excellent rate performance, characterized by rapid charging and discharging capability.

CONCLUSIONS

A simple and highly efficient electrodeposition method has been used to produce nanoflower-like hierarchical manganese oxide on carbon nanotubes (CNTs) grown on a flexible CF substrate. The utilization of a densely packed, highly porous

https://doi.org/10.1021/acsomega.4c07287
ACS Omega 2025, 10, 3439−3448

CNT forest enabled a substantial mass loading of MnO_2 necessary for practical applications. This binder-free nanostructured MnO_2@CNT composite electrode material showed excellent electrochemical energy storage capability, as evidenced by the results obtained from CV, GCD, and EIS experiments. The nearly rectangular shape observed in CV experiments at a faster scan rate (5−50 mV s^{-1}) and the triangular shape of the charge−discharge curve at the current densities (0.1 to 0.5 A g^{-1}) in GCD experiments demonstrate the capacitive nature of the MnO_2@CNT@CF electrode. The mass loading of MnO_2 on the electrode had a significant influence on the areal capacity and specific capacity. We observed that the highest specific capacitance of 219 F g^{-1} was achieved with a low mass loading (3.37 mg cm^{-2} using 65 square waves), while the highest areal capacitance of 1.5 F cm^{-2} was attained with a high mass loading (15.6 mg cm^{-2} using 390 square waves) in a half-cell configuration. Furthermore, when examining a symmetric cell in coin cell configuration with 65 square wave electrodes, we found that it retained 88% of its initial capacity even after 7000 cycles. This indicates the excellent stability of the electrode over extended cycling. Additionally, EIS revealed fast charge transfer kinetics characterized by a low charge transfer resistance of less than an ohm. Moreover, the absence of a visible 45° region in the Nyquist plot, typically associated with Warburg or diffusion resistance, indicated the easy diffusion of ions into the electrode. This can be attributed to the nanoflower-like structure of MnO_2, which is supported on porous CNTs. The incorporation of MnO_2 and CNTs holds great potential for the development of high-capacity, fast-charging, and reliable supercapacitors suitable for various applications, including electric vehicles, cell phones, and other devices requiring fast charging.

AUTHOR INFORMATION

Corresponding Author

Tara P. Dhakal − *Center for Autonomous Solar Power (CASP), Department of Electrical and Computer Engineering, and Materials Science and Engineering, Binghamton University, Binghamton, New York 13902, United States;* orcid.org/0000-0003-0885-3254; Email: tdhakal@binghamton.edu

Authors

Mahesh Nepal − *Center for Autonomous Solar Power (CASP) and Department of Electrical and Computer Engineering, Binghamton University, Binghamton, New York 13902, United States;* orcid.org/0009-0004-6971-0032

Ganesh Sainadh Gudavalli − *Center for Autonomous Solar Power (CASP) and Department of Electrical and Computer Engineering, Binghamton University, Binghamton, New York 13902, United States*

Complete contact information is available at: https://pubs.acs.org/10.1021/acsomega.4c07287

Author Contributions

The manuscript was written through contributions from all authors. Dhakal conceptualized the research, provided supervision of the investigation and measurement, and did a final review and editing.

Notes

The authors declare no competing financial interest.

ACKNOWLEDGMENTS

This work was in part supported by internal funding from the Thomas J. Watson College of Engineering and Applied Science at Binghamton University.

REFERENCES

(1) Şahin, M. E.; Blaabjerg, F.; Sangwongwanich, A. A Comprehensive Review on Supercapacitor Applications and Developments. *Energies 2022, Vol. 15, Page 674* **2022**, *15* (3), 674.

(2) Fischer, A. E.; Pettigrew, K. A.; Rolison, D. R.; Stroud, R. M.; Long, J. W. Incorporation of Homogeneous, Nanoscale MnO 2 within Ultraporous Carbon Structures via Self-Limiting Electroless Deposition: Implications for Electrochemical Capacitors. *Nano Lett.* **2007**, *7*, 281.

(3) Zhang, L. L.; Zhao, X. S. Carbon-Based Materials as Supercapacitor Electrodes. *Chem. Soc. Rev.* **2009**, *38* (9), 2520−2531.

(4) Brousse, T.; Belanger, D.; Long, J. W. To Be or Not To Be Pseudocapacitive? *J. Electrochem. Soc.* **2015**, *162* (5), A5185−A5189.

(5) Lee, B. J.; Sivakkumar, S. R.; Ko, J. M.; Kim, J. H.; Jo, S. M.; Kim, D. Y. Carbon Nanofibre/Hydrous RuO2 Nanocomposite Electrodes for Supercapacitors. *J. Power Sources* **2007**, *168* (2), 546−552.

(6) Biswal, A.; Tripathy, B. C.; Sanjay, K.; Subbaiah, T.; Minakshi, M. Electrolytic Manganese Dioxide (EMD): A Perspective on Worldwide Production, Reserves and Its Role in Electrochemistry. *RSC Adv.* **2015**, *5* (72), 58255−58283.

(7) Barclay, M.; Firestein, K.; Wang, X.; Motta, N.; Dubal, D.; Ostrikov, K. Plasma-Activated Water for Improved Intercalation and Pseudocapacitance of MnO2 Supercapacitor Electrodes. *Materials Today Sustainability* **2023**, *22*, No. 100388.

(8) Cao, F.; Pan, G. X.; Xia, X. H.; Tang, P. S.; Chen, H. F. Synthesis of Hierarchical Porous NiO Nanotube Arrays for Supercapacitor Application. *J. Power Sources* **2014**, *264*, 161−167.

(9) Xiang, C.; Li, M.; Zhi, M.; Manivannan, A.; Wu, N. A Reduced Graphene Oxide/Co3O4 Composite for Supercapacitor Electrode. *J. Power Sources* **2013**, *226*, 65−70.

(10) Joseph, N.; Shafi, P. M.; Bose, A. C. Recent Advances in 2D-MoS2 and Its Composite Nanostructures for Supercapacitor Electrode Application. *Energy Fuels* **2020**, *34* (6), 6558−6597.

(11) Nabi, G.; Riaz, K. N.; Nazir, M.; Raza, W.; Tahir, M. B.; Rafique, M.; Malik, N.; Siddiqa, A.; Ali Gillani, S. S.; Rizwan, M.; Shakil, M.; Tanveer, M. Cogent Synergic Effect of TiS2/g-C3N4 Composite with Enhanced Electrochemical Performance for Supercapacitor. *Ceram. Int.* **2020**, *46* (17), 27601−27607.

(12) Huang, S.; Bi, D.; Xia, Y.; Lin, H. Facile Construction of Three-Dimensional Architectures of a Nanostructured Polypyrrole on Carbon Nanotube Fibers and Their Effect on Supercapacitor Performance. *ACS Appl. Energy Mater.* **2023**, *6* (2), 856−864.

(13) Shaheen Shah, S.; Oladepo, S.; Ali Ehsan, M.; Iali, W.; Alenaizan, A.; Nahid Siddiqui, M.; Oyama, M.; Al-Betar, A. R.; Aziz, M. A. Recent Progress in Polyaniline and Its Composites for Supercapacitors. *Chem. Rec.* **2024**, *24* (1), No. e202300105.

(14) Chen, Y.; Yang, H.; Han, Z.; Bo, Z.; Yan, J.; Cen, K.; Ostrikov, K. K. MXene-Based Electrodes for Supercapacitor Energy Storage. *Energy Fuels* **2022**, *36* (5), 2390−2406.

(15) Wang, S.; Ma, Y.; Zhu, S.; Ma, H.; Yue, Y.; Wu, Q.; Xiao, H.; Han, J. Biomimetic and Electrostatic Self-Assembled Nanocellulose/MXene Films Constructed with Sequential Bridging Strategy for Flexible Supercapacitor. *Chemical Engineering Journal* **2024**, *495*, No. 153552.

(16) Zhu, S.; Chen, M.; Wang, S.; Wu, W.; Yue, Y.; Fu, Q.; Jiang, S.; He, S.; Wu, Q.; Xiao, H.; Han, J. Boosting Photothermal Conversion and Energy Storage in MXene Electrodes through Softened Wood toward Solar-Enhanced Flexible Supercapacitor. *Ind. Crops Prod* **2024**, *221*, No. 119289.

(17) Lee, S. W.; Kim, J.; Chen, S.; Hammond, P. T.; Shao-Horn, Y. Carbon Nanotube/Manganese Oxide Ultrathin Film Electrodes for Electrochemical Capacitors. *ACS Nano* **2010**, *4* (7), 3889−3896.

(18) Lee, H. Y.; Goodenough, J. B. B. Supercapacitor Behavior with KCl Electrolyte. *J. Solid State Chem.* **1999**, *144* (1), 220−223.
(19) Liu, L.; Su, L.; Lu, Y.; Zhang, Q.; Zhang, L.; Lei, S.; Shi, S.; Levi, M. D.; Yan, X. The Origin of Electrochemical Actuation of MnO2/Ni Bilayer Film Derived by Redox Pseudocapacitive Process. *Adv. Funct Mater.* **2019**, *29* (8), No. 1806778.
(20) Zhang, Q. Z.; Zhang, D.; Miao, Z. C.; Zhang, X. L.; Chou, S. L. Research Progress in MnO2−Carbon Based Supercapacitor Electrode Materials. *Small* **2018**, *14* (24), No. 1702883.
(21) Cao, J.; Wang, Y.; Zhou, Y.; Ouyang, J. H.; Jia, D.; Guo, L. High Voltage Asymmetric Supercapacitor Based on MnO2 and Graphene Electrodes. *J. Electroanal. Chem.* **2013**, *689*, 201−206.
(22) Tan, D. Z. W.; Cheng, H.; Nguyen, S. T.; Duong, H. M. Controlled Synthesis of MnO2/CNT Nanocomposites for Supercapacitor Applications. *Mater. Technol.* **2014**, *9* (3), A107−A113.
(23) Zhou, Y.; Cheng, X.; Tynan, B.; Sha, Z.; Huang, F.; Islam, M. S.; Zhang, J.; Rider, A. N.; Dai, L.; Chu, D.; Wang, D. W.; Han, Z.; Wang, C. H. High-Performance Hierarchical MnO2/CNT Electrode for Multifunctional Supercapacitors. *Carbon N Y* **2021**, *184*, 504−513.
(24) Zhang, H.; Cao, G.; Wang, Z.; Yang, Y.; Shi, Z.; Gu, Z. Growth of Manganese Oxide Nanoflowers on Vertically-Aligned Carbon Nanotube Arrays for High-Rate Electrochemical Capacitive Energy Storage. *Nano Lett.* **2019**, *8*, 2664.
(25) Kour, S.; Tanwar, S.; Sharma, A. L. MnO2 Nanorod Loaded Activated Carbon for High-Performance Supercapacitors. *J. Alloys Compd.* **2022**, *910*, No. 164834.
(26) Bai, X. L.; Gao, Y. L.; Gao, Z. Y.; Ma, J. Y.; Tong, X. L.; Sun, H. B.; Wang, J. A. Supercapacitor Performance of 3D-Graphene/MnO2foam Synthesized via the Combination of Chemical Vapor Deposition with Hydrothermal Method. *Appl. Phys. Lett.* **2020**, *117* (18), No. 183901.
(27) Dawoud, H. D.; Al Tahtamouni, T.; Bensalah, N. Sputtered Manganese Oxide Thin Film on Carbon Nanotubes Sheet as a Flexible and Binder-Free Electrode for Supercapacitors. *Int. J. Energy Res.* **2019**, *43* (3), 1245−1254.
(28) Li, L.; Hu, Z. A.; An, N.; Yang, Y. Y.; Li, Z. M.; Wu, H. Y. Facile Synthesis of MnO2/CNTs Composite for Supercapacitor Electrodes with Long Cycle Stability. *J. Phys. Chem. C* **2014**, *118* (40), 22865−22872.
(29) Liu, X.; Yi, X.; Zhang, J.; Zhao, X.; Liu, S.; Wang, T.; Cui, S. Synthetic Strategy for MnO2 Nanoparticle/Carbon Aerogel Heterostructures for Improved Supercapacitor Performance. *ACS Appl. Nano Mater.* **2023**, *6* (15), 14127−14135.
(30) Rajbhandari, P. P.; Dhakal, T. P. Low Temperature ALD Growth Optimization of ZnO, TiO2, and Al2O3 to Be Used as a Buffer Layer in Perovskite Solar Cells. *J. Vac. Sci. Technol., A* **2020**, *38*, No. 032406.
(31) Gudavalli, G. S.; Nepal, M.; Young, J.; Smeu, M.; Dhakal, T. P. Effect of a Ti Layer on the Growth of Binder-Free Carbon Nanotubes on Cu Foil and Their Performance as Lithium Ion Battery Anodes. *Energy Advances* **2023**, *2* (8), 1182−1189.
(32) Gudavalli, G. S.; Turner, J. N.; Dhakal, T. P. Chemical Vapor-Deposited Carbon Nanotubes as Electrode Material for Supercapacitor Applications. *MRS Adv.* **2017**, *2* (54), 3263−3269.
(33) Niu, C.; Sichel, E. K.; Hoch, R.; Moy, D.; Tennent, H. High Power Electrochemical Capacitors Based on Carbon Nanotube Electrodes. *Appl. Phys. Lett.* **1997**, *70* (11), 1480.
(34) Mkhondo, N. B.; Magadzu, T. Effects of Different Acid-Treatment on the Nanostructure and Performance of Carbon Nanotubes in Electrochemical Hydrogen Storage. *Dig. J. Nanomater. Biostructures* **2014**, *9* (4), 1331−1338.
(35) Gao, Y.; Pandey, G. P.; Turner, J.; Westgate, C. R.; Sammakia, B. Chemical Vapor-Deposited Carbon Nanofibers on Carbon Fabric for Supercapacitor Electrode Applications. *Nanoscale Res. Lett.* **2012**, *7* (1), 651.
(36) Pan, H.; Li, J.; Feng, Y. P. Carbon Nanotubes for Supercapacitor. *Nanoscale Res. Lett.* **2010**, *5* (3), 654−668.
(37) Adelkhani, H. Functionalized Electrolytic Manganese Dioxide Nanostructure Prepared at Fixed PH for Electrochemical Supercapacitor. *J. Electrochem. Soc.* **2009**, *156* (10), A791.
(38) David, L.; Dahlberg, K.; Mohanty, D.; Ruther, R. E.; Huq, A.; Chi, M.; An, S. J.; Mao, C.; King, D. M.; Stevenson, L.; Wood, D. L. III Unveiling the Role of Al2O3 in Preventing Surface Reconstruction during High-Voltage Cycling of Lithium-Ion Batteries. *ACS Appl. Energy Mater.* **2019**, *2* (2), 1308−1313.
(39) Adusumilli, S. P.; Westgate, C. R. Factors Affecting the Growth Behavior of De-Ionized Water Assisted Carbon Nanotube Forests. *J. Nanosci Nanotechnol* **2015**, *15* (9), 6609−6616.
(40) Gudavalli, G. S.; Turner, J. N.; Dhakal, T. P. Pulse Electrodeposited Manganese Oxide on Carbon Fibers as Electrodes for High Capacity Supercapacitors. *Nanotechnology* **2019**, *30*, No. 455701.
(41) Xu, B.; Ye, M.-L.; Yu, Y.-X.; Zhang, W.-D. A Highly Sensitive Hydrogen Peroxide Amperometric Sensor Based on MnO 2-Modified Vertically Aligned Multiwalled Carbon Nanotubes. *Anal. Chim. Acta* **2010**, *674*, 20−26.
(42) Luo, L.; Meng, W.; Wang, G.; Qin, J.; He, H.; Huang, H. MnO2 Nanoflowers-Decorated MXene Nanosheets with Enhanced Supercapacitor Performance. *J. Alloys Compd.* **2023**, *957*, No. 170411.
(43) Mothkuri, S.; Gupta, H.; Jain, P. K.; Rao, T. N.; Padmanabham, G.; Chakrabarti, S. Functionalized Carbon Nanotube and MnO2 nanoflower Hybrid as an Electrode Material for Supercapacitor Application. *Micromachines 2021, Vol. 12, Page 213* **2021**, *12* (2), 213.
(44) Jiang, Y.; Ling, X.; Jiao, Z.; Li, L.; Ma, Q.; Wu, M.; Chu, Y.; Zhao, B. Flexible of Multiwalled Carbon Nanotubes/Manganese Dioxide Nanoflake Textiles for High-Performance Electrochemical Capacitors. *Electrochim. Acta* **2015**, *153*, 246−253.
(45) Baptista, J.; Shacklock, J.; Shaban, M.; Alkayal, A.; Lobato, K.; Wijayantha, U. Superior Rate Capability of High Mass Loading Supercapacitors Fabricated with Carbon Recovered from Methane Cracking. *Inorganics 2023, Vol. 11, Page 316* **2023**, *11* (8), 316.
(46) Wei, W.; Cui, X.; Chen, W.; Ivey, D. G. Electrochemical Cyclability Mechanism for MnO2 Electrodes Utilized as Electrochemical Supercapacitors. *J. Power Sources* **2009**, *186* (2), 543−550.
(47) Gong, Y.; Li, D.; Fu, Q.; Pan, C. Influence of Graphene Microstructures on Electrochemical Performance for Supercapacitors. *Progress in Natural Science: Materials International* **2015**, *25* (5), 379−385.
(48) Li, Z.; Liu, J.; Qin, Y.; Gao, T. Enhancing the Charging Performance of Lithium-Ion Batteries by Reducing SEI and Charge Transfer Resistances. *ACS Appl. Mater. Interfaces* **2022**, *14* (29), 33004−33012.

https://doi.org/10.1021/acsomega.4c07287
ACS Omega 2025, 10, 3439−3448